

# Journal of Biomedical Optics

[SPIDigitalLibrary.org/jbo](http://SPIDigitalLibrary.org/jbo)

## **Feasibility study on bonding quality inspection of microfluidic devices by optical coherence tomography**

Shiguang Li  
Zhiguang Xu  
Soon Fatt Yoon  
Zhong Ping Fang

# Feasibility study on bonding quality inspection of microfluidic devices by optical coherence tomography

Shiguang Li,<sup>a,b,c</sup> Zhiguang Xu,<sup>a,b,c,d</sup> Soon Fatt Yoon,<sup>a,b</sup> and Zhong Ping Fang<sup>c</sup>

<sup>a</sup>Singapore-MIT Alliance, N3.2-01-36, 65 Nanyang Drive, Singapore 637460

<sup>b</sup>Nanyang Technological University, School of Electrical and Electronic Engineering, Singapore 639798

<sup>c</sup>Singapore Institute of Manufacturing Technology, 71 Nanyang Drive, Singapore 638075

<sup>d</sup>Massachusetts Institute of Technology, 77 Massachusetts Avenue, Cambridge, Massachusetts 02139

**Abstract.** This paper reports the feasibility of optical coherence tomography (OCT) technology for inspection of bonding quality of microfluidic devices in manufacturing environments. A compact optical-fiber-based OCT is developed and its measurement performance is characterized. A series of microfluidic devices respectively bonded by adhesive tape, thermal method, and oxygen plasma, are inspected. The defects of geometry deformation and sealing completeness are emphasized during measurements. Based on the inspection results, some discoveries related to the production of microfluidic devices are discussed. © 2011 Society of Photo-Optical Instrumentation Engineers (SPIE). [DOI: 10.1117/1.3590747]

Keywords: optical coherence tomography; microfluidic device; bonding quality inspection; deformation; buried structure.

Paper 10524RR received Sep. 27, 2010; revised manuscript received Apr. 21, 2011; accepted for publication Apr. 22, 2011; published online Jun. 2, 2011.

## 1 Introduction

With the fast development of micromanufacturing technology, miniaturization of traditionally large system(s) on a microchip becomes possible. As one of the most successful implements, microfluidic devices are a group of microdevices on which a small amount of fluid is precisely contained, mixed, and controlled. Such devices have found wide applications in biology, chemistry, optics, and many other areas where a tiny volume of fluid is preferred or critical.<sup>1,2</sup> The polymer-based microfluidic devices have shown to be very promising because of the low cost and high convenience for mass production. In the production of microfluidic devices, bonding is often the last and the most important processing step, so it significantly affects the final performance of the devices. For example, the bonding strength determines the reliability of the device and the maximum driving pressure of the microflow; the sealing incompleteness results in fluid leakage; the geometry deformation of microchannels affects the flowing status and speed or even blocks the fluid flow; the variability of the channels' cross sectional area has an important impact on the hydrodynamic dispersion of the flow inside the channels.<sup>3</sup> Thus, it is necessary to inspect the bonding quality of microfluidic devices during the manufacturing process. Bonding of microfluidic devices can be classified into two categories: 1. bonding a patterned layer with a cover plate to form a single-layer chip, and 2. sandwiching and sealing several patterned layers into a multiple-layer device. The common bonding methodologies include thermal bonding,<sup>4</sup> plasma bonding,<sup>5</sup> solvent bonding,<sup>6</sup> UV bonding,<sup>7</sup> adhesive tape bonding,<sup>8,9</sup> etc.

Because of the inherent transparency of the polymer materials, optical tools naturally become the dominant approaches in bonding inspection (excluding the bonding strength characterization which is quite different from what will be discussed

in this paper). Currently, the optical microscope and camera are most popularly employed, which can quickly find the incomplete bonding area by observing either the irregular channel boundary or the interference caused colorful equal-thickness fringes. To quantify the geometry deformation of a micropattern under a piece of cover layer, the laser confocal sensor that is able to measure the transparent objective thickness<sup>10</sup> or optical interferometric profiler with through transmissive media module<sup>11</sup> can be applied. However, these two techniques are not able to measure the multilayer microfluidic devices. In recent years, optical coherence tomography (OCT) has been widely applied in biomedical areas for noninvasive imaging of deep tissues.<sup>12,13</sup> It is also employed to obtain the three-dimensional velocity or structural image when scattering liquid flows in the bonded microfluidic devices.<sup>14</sup> However, the application of OCT in the manufacturing industry is rarely reported. In this paper, we will introduce a compact fiber-based OCT device and investigate its feasibility to nondestructively inspect the bonding quality of microfluidic devices in production environments. Two issues will be emphasized: 1. measurement of geometry deformation of microfluidic devices during bonding and 2. inspection of sealing completeness at the bonding interface.

## 2 Experimental Setup

The OCT setup is illustrated in Fig. 1(a). The light from a superluminescent laser diode (Superlum, Ireland) with a central wavelength of 835 nm, bandwidth of 50 nm, and output power of 1.25 mW is coupled into a single mode fiber. After passing through a 3 dB coupler, half of the light is incident onto a fixed reference mirror through a collimator, forming the reference arm of the OCT, and the other half is guided into the sample through an identical collimator and an achromatic

Address all correspondence to: Shiguang Li; E-mail: lishiguang@tsinghua.org.cn.

1083-3668/2011/16(6)/066011/9/\$25.00 © 2011 SPIE

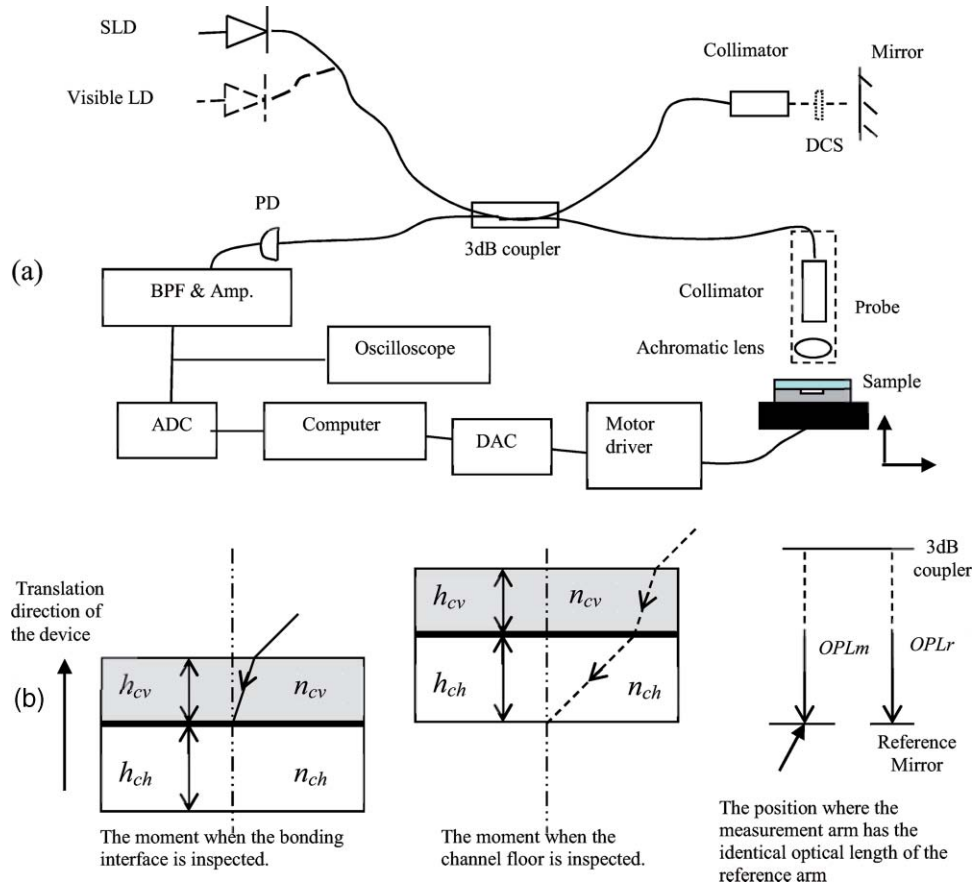


**Fig. 1** (a) Schematic diagram of OCT. SLD: superluminescent laser diode, BPF: band pass filter, Amp: amplifier, PD: photodiode, ADC: analog/digital converter, DAC: digital/analog converter. DCS: dispersion compensation slide. The arrow2 close to the sample represents the scanning directions of the motor stage. The measurement probe consists of a pigtailed collimator and an achromatic lens. (b) Scanning process at the bonding interface.

focusing lens, functioning as the measurement arm. The light beams reflected from the two arms recombine and approach a photodetector (New Focus Model: 2107), where the two optical beams interfere with each other. The detector is composed of a photodiode for light detection as well as a gain circuit for signal amplification. The signal is processed with a band-pass filter with a frequency bandwidth of 10 Hz to 10 KHz for the signal-to-noise ratio (SNR) improvement. The filtered signal is then amplified and digitalized by an analog/digital converter (ADC), and transferred to a computer for further signal processing. An oscilloscope is used for direct observation and a supplementary visible laser diode (LD) is used for optical alignment. In experiments, the sample under testing is scanned along the vertical axial, and then moves one step along the lateral axis by a computer-controlled two-dimensional translation stage. By acquiring the signal from each scanning point, the cross-sectional tomographic image of the microfluidic devices is constructed.

Figure 1(b) shows the details about the scanning process at the bonding interface and the buried channel. The solid gray rectangle represents the cover layer and the white one is the channel. The bonding interface, i.e., the bottom surface of the cover layer or the channel top, is indicated as a bold line.  $h_{cv}$  and  $h_{ch}$ , respectively, represent the heights of the cover layer and the channel.  $n_{cv}$  and  $n_{ch}$  are the refractive indices of the cover layer and the medium inside the channel.  $n_{ch}$  is 1 when the channel

is filled with air.  $OPL_r$  is the optical path length between the reference mirror and the 3 dB coupler, and  $OPL_m$  is the optical path length between the measured interface and the coupler. Due to the low coherence interference of OCT, the constructive interference fringes can be formed only when the difference between  $OPL_r$  and  $OPL_m$  is within the coherence length of the applied superluminescent laser diode. Since the cover plate and the substrate of the patterned polymer layer are both highly homogenous in optical property, only the light reflected from the bonding interface and the channel floor contributes to the interferometric signal. The translation distance between two sharp interference signals is the channel depth. From the plot it can be seen that the focal plane remains the same when measuring the bonding interface and the channel floor if  $OPL_r$  is a constant and  $n_{ch} = 1$ .

### 3 Measurement Results

A series of microfluidic devices bonded by adhesive tape, thermal method, and oxygen plasma techniques are measured by means of the OCT.

#### 3.1 Inspection for Adhesive Tape Bonding

A microfluidic device bonded with adhesive tape was fabricated and characterized. A piece of adhesive tape was sandwiched between the cover layer and the patterned layer, and then the

**Table 1** Bonding parameters and the device structure.

Specifications		Figure 2	Figure 3	Figure 4
Bonding method		Adhesive tape	Thermal bonding	Oxygen plasma
Cover layer	Material	PC	PC	PDMS
	Thickness	0.5 mm	1.5 mm	4 mm
Patterned layer material		PC	PC	PDMS
Designed channel size		600 × 300	500 × 300	150 × 50
(Width × Depth, unit: $\mu\text{m}$ )				

stack was pressed with a pressing roller at room temperature to tightly bond the two layers together. The detailed bonding parameters can be found in Table 1. Figure 2(a) schematically illustrates the measured region including two buried channels. The signal variation of the direct tomographic image is too immense to find details as shown in Fig. 2(d), whose reason is to be explained in Sec. 4.2. To highlight the deep sub-surfaces, the measured data was normalized along the depth direction at each interface region, i.e., the bonding interface and the channel floor regions for this device. To concentrate on the bonding inspection results presented here, the data normalization process is discussed in Sec. 4.2. The image after processing is shown in Fig. 2(b). In the image, the interface is evident and the adhesive tape between the two layers is clearly identified. The abnormal data inconsistency at the depth of 150  $\mu\text{m}$  is caused by the data separation procedure during normalization. It does not affect inspection as long as the inspector knows the data normalization process. The noise occurs where there is no evident signal peak along the normalization direction, that is, there is no evident feature along the depth direction. The cover layer on top of the channel is deformed and sunk into the hollow space of the microchannel. This deformation should be caused by a large amount of pressure exerted during bonding. Another defect is found in one of the channel walls which is circled with a dashed line. The geometry distortion of the channel floor is not evident. The microchannels' sidewall is invisible because there is almost no light reflected back to the detector. To accurately quantify the geometry deformation of the buried channel, the profile of the buried microchannel is extracted, as shown in Fig. 2(c). The extraction algorithm is introduced in Sec. 4.3. The channel depth after bonding is quantified as 322  $\mu\text{m}$ , larger than the designed value of 300  $\mu\text{m}$ .

### 3.2 Inspection for Thermal Bonding

Similarly, a microfluidic device bonded with a thermal method was made for inspection. The bonding parameters are listed in Table 1. The patterned substrate and the cover plate were bonded at 139°C at the pressure of 2.6 MPa and then cooled at room temperature before unloading. Figure 3(a) illustrates the measured region with one channel, Fig. 3(b) shows the tomographic image, and Fig. 3(c) shows the channel's profile. The dataset separation position for normalization is at a depth of 430  $\mu\text{m}$ . The significant difference of Fig. 3(b) from Fig. 2(b) is that the

bonding interface between the cover plate and the channeled substrate disappears. This is because the two bonded layers are made from the same material, namely, polycarbonate (PC). As two pieces with the same material are perfectly bonded together, there is no intermediate layer or interface between the two layers to reflect the light. This provides a criterion to judge whether the two layers made of the same material are bonded in high quality or not. The channel depth is estimated as 275  $\mu\text{m}$  in Fig. 3(c), which is less than the designed value of 300  $\mu\text{m}$ . This is caused by the thermal shrinkage of the polymer material and high process pressure. For comparison, Fig. 3(d) shows another sample bonded in the same condition. Two evident interfaces appear at a depth close to 500  $\mu\text{m}$ , indicating that the two layers are detached even though they seem tightly bonded by visual observation. The upper interface represents the bottom surface of the cover layer and the lower interface represents the top surface of the patterned layer. From the measured image, one can see that the cover layer becomes curved after bonding. The air gap about 20  $\mu\text{m}$  between the two layers can be detected by measuring the signal peak positions at the two interfaces.

### 3.3 Inspection for Plasma Bonding

Another microfluidic device, fabricated by soft lithography and then bonded with the oxygen plasma method, was also measured. Figure 4(a) shows the schematic illustration of the device. The patterned layer was made by pouring the liquid polydimethylsiloxane (PDMS) with a curing agent over the silicon mold, and then peeled off from the mold after solidification. The patterned surface and the PDMS cover layer were treated for 30 s at the power of 100 W oxygen plasma, and then were immediately joined together. In order to strengthen the bonding quality, the sample was placed into an oven for 15 min at 80°C.<sup>15</sup> The detailed bonding parameters are listed in Table 1.

The first measurement result indicates that the signal intensity from the sample, i.e., the dc signal component, was evident. However, there was no interference signal until a compensation slide identical to the cover layer was inserted between the reference collimator and the mirror. This is because the chromatic dispersion arising from the 4-mm thick cover layer prevents the formation of the interference signal. The compensation slide in the reference arm was adopted to balance the optical dispersion of the cover layer. Certainly, the tradeoff is the intensity loss of the reference arm induced by the uncoated compensation slide,

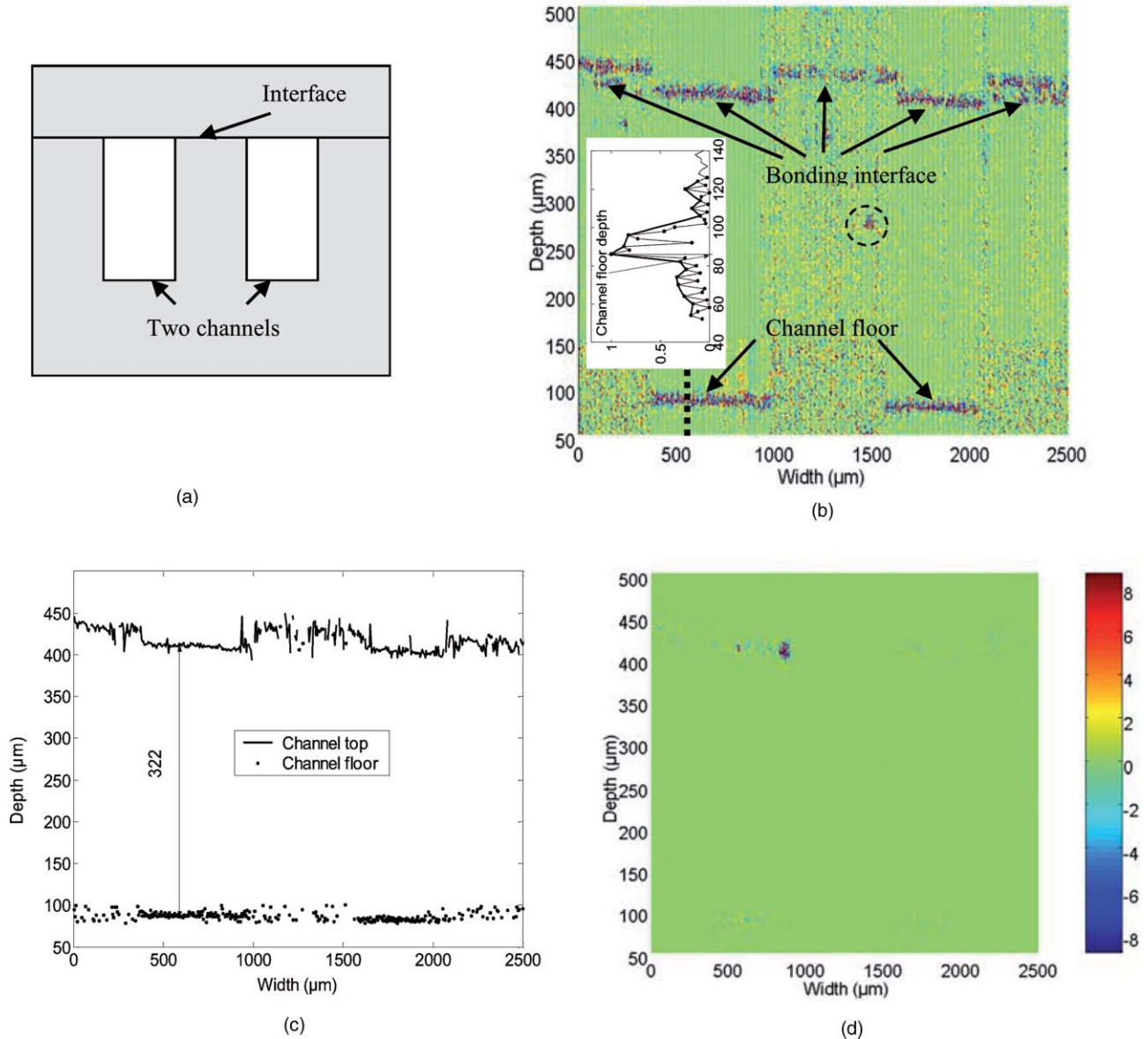


**Fig. 2** Measurement results of a microfluidic device bonded with adhesive tape. (a) Illustration of the measured region; (b) normalized tomographic image; (c) profile of the microchannel; (d) raw tomographic image. In the normalized image, the generally vertical distributed noise occurs wherever there is no evident feature along the axial scanning direction. The position where there is sudden data inconsistency, i.e., at depth 150  $\mu\text{m}$ , is the position for subsets separation. The scale unit in all images in this paper is micrometers. The lateral axis is the width direction and the vertical axis is the depth direction. The color in (b) represents the normalized signal amplitude, and in (d) is the signal amplitude in unit of volts.

which reduces the signal amplification in this OCT. The analysis on how the reference beam affects the signal amplification can be found in Sec. 4.1. Figure 4(b) is the acquired tomographic image of the device. A great deal of information regarding the channel top is missing, and the channel floor is more evident than the channel top, although the channel floor is deeper. This indicates, 1. 4 mm is close to the maximum thickness of the PDMS cover layer in which this OCT can feasibly characterize; 2. the collected light from the channel floor is greater than that from the channel top. One potential reason for 2. is that the channel floor is rougher than the channel top. The surface quality of the channel floor is degraded by the mold roughness and the peeling process, and therefore is rougher than the naturally smooth blank cover layer, i.e., the channel top in the bonded

device. As there is evident optical aberration when measuring the deep features, only a small portion of light strictly focuses on the channel top or floor. For the very smooth channel top, the nonfocusing light is not able to be reflected into fiber due to the specular reflection; while for the rougher channel floor, some nonfocusing light is still able to be collected due to backscattering. To improve the image quality of such features under a thick layer, the dynamic focusing technique<sup>16</sup> or focus tracking technique<sup>17</sup> is applied, which will be the emphasis in our future work.

### 3.4 Inspection for Heterogeneous Devices

To evaluate the feasibility of our OCT for characterizing various bonding methodologies, the bonded samples with high diversity

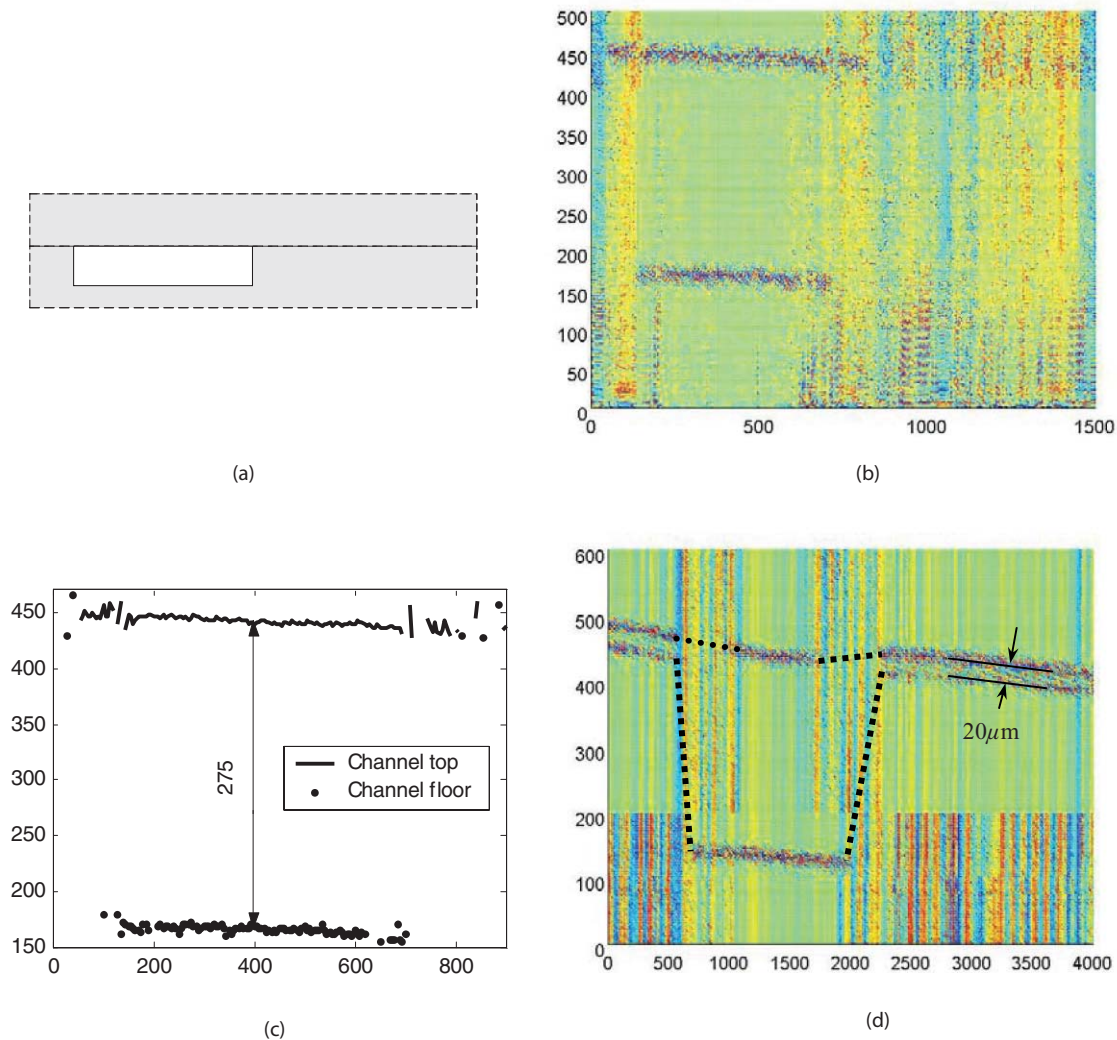


**Fig. 3** Measurement results of a microfluidic device bonded with thermal method. (a) Illustration of the measured region; (b) normalized tomographic image; (c) profile of the microchannel; (d) tomographic image of a detached microfluidic device. The dotted lines are the presumed geometry on either channel top or sidewall where the light is too weak to be detected.

in dimensions, materials, and bonding parameters were measured. Some of them are shown in Fig. 5. Figure 5(a) shows the bonding interface of a poly(methylmethacrylate) (PMMA) sample bonded with a thermal method. The microchannels are  $50\ \mu\text{m}$  wide and  $10\ \mu\text{m}$  deep, covered by a 1.5-mm thick plate. The two layers are thermally bonded at  $104^\circ\text{C}$  under a pressure of about 3 MPa for 1 min before cooling to about  $60^\circ\text{C}$  and unloading. From the image, it can be seen that the two layers are detached because the interface between the bonded layers is clearly visible. Though the channel shape is not very clear, the two channels can still be identified as circled with dashed lines, the right of which is enlarged in the inset. Figure 5(b) show the bonding interface of another PMMA device with five different patterns. The channel depth is  $1\ \mu\text{m}$ , and the cover layer is still 1.5-mm thick. The interface was treated with plasma and then bonded at  $80^\circ\text{C}$  under 20 MPa for 2 min. Except for the five patterns, no evident features are found at the interface, indicating the two layers are bonded tightly together. However, the middle pattern is collapsed, i.e., the pattern top and floor contact with each other, indicating this bonding leads to some

geometry deformation. Figure 5(c) shows a PDMS microfluidic device bonded with plasma oxygen method. The cover layer is only about  $20\text{-}\mu\text{m}$  thick. The imaged line at a depth of  $\sim 140\ \mu\text{m}$  is the top surface of the cover layer, while a short line at the depth less than  $100\ \mu\text{m}$  is the channel. The dashed line is the presumed bonding interface. The data separation position for image normalization is at  $100\ \mu\text{m}$ . There is no signal found at the bonding interface, indicating the two layers are well bonded.

## 4 Discussion

### 4.1 System Sensitivity and SNR

As the signal from the interface is weak, the system sensitivity is crucial for this application. In experiments, a high-quality dc filter is employed to remove the dc component from the output of the photodetector. According to the interference principle, the amplitude of the alternate component (ac) signal is:

$$V_{\text{output}} = 2 \cdot G \cdot R \cdot k \sqrt{I_1 I_2} \quad (1)$$

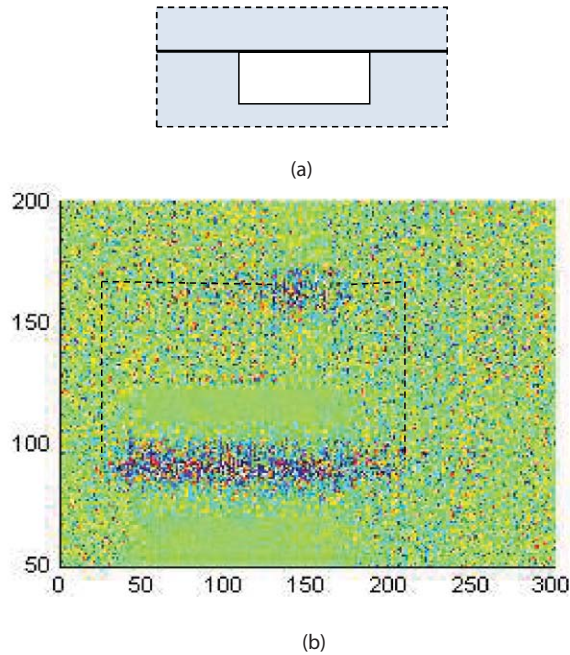


**Fig. 4** Measurement results of a microfluidic device bonded with oxygen plasma method. (a) Illustration of the measured region; (b) normalized tomographic image. The dashed line is the presumed geometry.

where  $R$  is the response efficiency of the photodiode in unit V/mW and  $G$  is the magnification factor of the gain circuit in the detector;  $I_1$  and  $I_2$  is the light intensity on the photodiode from the reference and sample beams, respectively;  $k$  is an experimental coefficient of about 0.5 induced by the mismatch of the states of polarization between the two beams. To achieve sufficient  $V_{\text{output}}$  to detect the weak signal of  $I_2$ ,  $I_1$  has to be adjusted to a relatively high value, at least much greater than  $I_2$ , according to Eq. (1). In other words,  $I_1$  functions as an optical amplifier in the OCT, similar to that in the optical heterodyne detection system.<sup>18</sup> This could explain why the intensity loss in the reference arm results in evident reduction of signal amplification in Fig. 4(b). However, for avoiding the signal saturation during measurements,  $I_1$  cannot be infinitely large. Possibly because of the internal circuit design of the detector, the experiments showed that there is an ac signal only when

$$V_{\text{dc}}/30 < V_{\text{sat}}, \quad (2)$$

where  $V_{\text{sat}}$  is the saturation voltage 8.8 V, and  $V_{\text{dc}}$  is the voltage output when the two optical beams do not interfere, i.e.,

$$V_{\text{dc}} = G \cdot R \cdot (I_1 + I_2) \quad (3)$$

Actually,  $V_{\text{dc}}/30$  is an electrical setting built in the photodetector, which we often used to do preliminary alignment before finding the interference signal.

Substituting Eq. (3) into Eq. (2), we have

$$I_1 < \frac{30V_{\text{sat}}}{G \cdot R} - I_2. \quad (4)$$

$G$  is often set as the maximum value  $3 \times 10^4$ ;  $R$  is about 0.33 V/mW; and  $I_2$  is neglectable as it is much smaller than  $I_1$ . According to Eq. (4),  $I_1$  has to be less than 26.7  $\mu\text{W}$ .

On the other hand, to detect the interference signal,  $V_{\text{output}}$  has to be:

$$V_{\text{output}} > V_{\text{noise}}, \quad (5)$$

where  $V_{\text{noise}}$  is the voltage noise of the detector, which is experimentally determined as 10 mV (standard deviation value) in the frequency range of 10 Hz to 10 KHz. Substituting Eq. (1) into Eq. (5), we have

$$I_2 > \left( \frac{V_{\text{noise}}}{2k \cdot G \cdot R} \right)^2 / I_1. \quad (6)$$

Considering  $I_1 < 26.7 \mu\text{W}$ ,  $G = 3 \times 10^4$ ,  $R = 0.33 \text{ V/mW}$ , and  $k \approx 0.5$ , the minimum  $I_2$  is about 0.04 pW, i.e., the system sensitivity is 0.04 pW. It should be noted that this value does not consider the loss from the sample to the fiber end and from the fiber end to the detector.

To measure the SNR, a mirror often replaces the sample to get the maximum signal.<sup>19</sup> In our experiment, the maximum signal is the saturation voltage 8.8 V. Considering the system noise is 10 mV, the system SNR is  $20 \lg(8.8 \text{ V}/10 \text{ mV}) = 59 \text{ dB}$ . In these experiments, the SNR is mainly limited by the low reflected light from the interface. In order to achieve an evident signal, we have to adopt greater reference intensity, which arouses greater beat noise<sup>20</sup> and shot noise.<sup>21</sup> The great reference intensity further results in great signal variation in one image, as discussed in Sec. 4.2. The most effective way to improve the SNR is to improve the collected light from the interface, as will be one of our future works.

#### 4.2 Great Signal Variation During Scanning and Signal Normalization in Image

The main difference between the measurements of biomedical tissues and microfluidic devices is that the majority of incident light from the smooth polymer surface/subsurface has specular reflection. Therefore, the light intensity collected by the single mode fiber is very directional sensitive. Since the surface/subsurface in the bonded devices is not strictly flat, the collected light from the sample varies during scanning. With the amplification of the reference beam, it is typical to record  $V_{\text{output}}$  from  $V_{\text{max}}$  (8.8 V) to  $V_{\text{min}}$  (10 mV) during one scanning. Such great signal variation results in observation difficulty in direct tomographic image such as in Fig. 2(d). The color represents the amplitude of  $V_{\text{output}}$  in unit of volts. Compared to Fig. 2(b), little information can be found in Fig. 2(d).

To make the deep structures evident for observation, we normalized the data set of  $V_{\text{output}}$  along the axial scanning direction (depth direction). With this method, the signal variation at different locations was minimized. Considering there is still a significant difference between different interfaces, such normalization was conducted at each interface. For example, there are two interfaces (bonding interface and channel floor) in Fig. 2. We divided into two subsets in Fig. 2(b), each of which included the data of the corresponding interface as well as its neighboring area. By the way, we have tried to use the logarithmic scale or other gray level way (i.e., remove strong signal out to emphasize the weak signal), but the features still are not all highlighted.

As a comparison,  $V_{\text{output}}$  is less sensitive to the perpendicularity between the probe axis and the measured surface

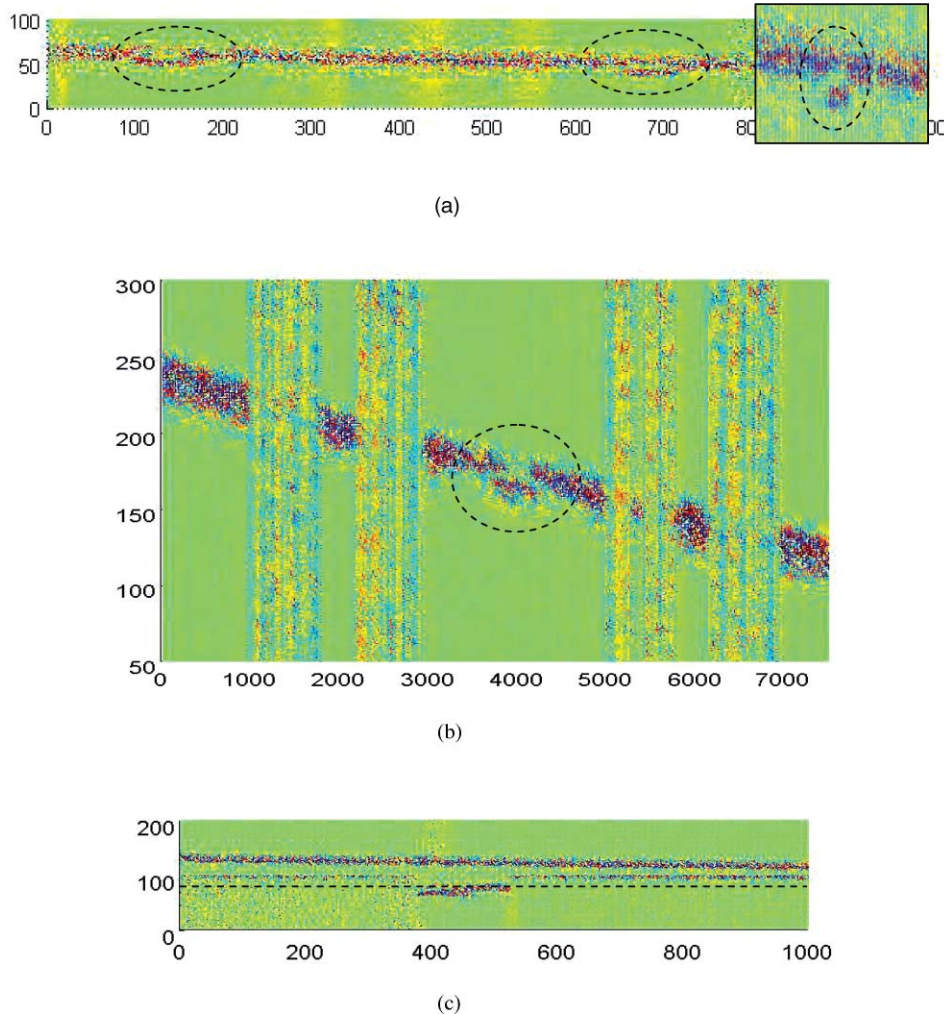


**Fig. 5** Tomographic image of (a) a detached interface with two microchannels bonded with thermal method; (b) a complete bonding interface with five micropatterns; (c) a microfluidic device bonded with oxygen plasma method. The circled region in (a) is two channels, the right of which is enlarged in the inset. The circled region in (b) is the collapsed region in the channel. The dashed line in (c) is the presumed bonding interface.

when measuring rough materials like paper or highly scattering materials like biological tissues. This is because there is still enough light collected into the fiber due to the light backscattering. Proved by sufficient experiments, such perpendicularity sensitivity is also decreased when the measurement probe consisting of a collimator and an achromatic lens is replaced by a single achromatic focuser. This can be taken into consideration when improving the OCT performance.

### 4.3 Profile Extraction of Buried Microstructure

Because the interface area of the microfluidic device reflects much more light than the neighboring homogeneous medium, the interferometric signal will form a localized peak when the measured optical path length equals the reference optical path length. One typical amplitude profile can be found in the inset of Fig. 2(b), which is the absolute value of the signal variation along the dashed line at the channel floor. The sub-peaks in the range of coherence length are evident even though they are less regular due to the signal instability during measurements. The intensity peak position is defined as the direct depth of the measured

interface similar to that in the typical white light profilometer.<sup>22</sup> By finding the series of peak positions at interfaces, the profile of the channel top and the floor was obtained in Fig. 2(c). One should note that the profile in Fig. 2(c) is the “direct profile” (or optical distance) from the tomographic image. According to the working principle of OCT, the physical distance between the two interfaces is the optical distance divided by the refractive index of the medium between the two interfaces. As the medium inside the channel is air, the real channel depth is the direct depth. For the cover layer, thickness is almost even, the bonding interface geometry presents its real profile.

### 4.4 Measurement Resolution and Repeatability

#### 4.4.1 In tomographic image

The vertical measurement resolution depends on the coherence length of the light source, which is calculated as  $6\ \mu\text{m}$  in air.<sup>23</sup> This value defines how far away between interfaces, e.g., channel top and floor, can be identified. For example, for the  $10\text{-}\mu\text{m}$  deep channel covered by a  $1.5\text{-mm}$  thick polymer in Fig. 5(a), the channel top and floor just can be identified by observing

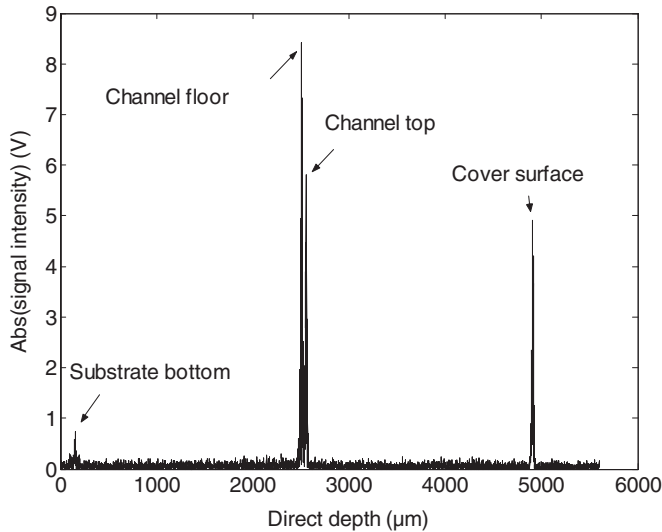


**Fig. 6** Signal varies along the axial direction of a microfluidic device at a certain position. The arrow is the scanning direction.

the inset. The lateral resolution (LR) mainly depends on the divergence angle of the collimator  $\theta$  and the focusing length of the optical lens  $f$ , according to the optical principle:  $LR = f\theta$ , assuming the output light from the collimator is strictly parallel and the LR is far greater than the diffraction limit. Due to the lack of  $\theta$ , the LR is estimated at about  $20\ \mu\text{m}$  by measuring some features in experiments.

#### 4.4.2 In topographic image

In case the distance between interfaces is greater than the depth resolution of the tomographic image, it is possible to obtain the topographic profile of each surface/subsurface with the method in Sec. 4.3. The profile's lateral resolution remains the same as that in the tomographic image, but the vertical resolution can achieve nanometers according to the white light interferometry principle.<sup>22</sup> The measurement repeatability was obtained as  $1.7\ \mu\text{m}$  by measuring the floor position at the dashed line in Fig. 2(b) five times and finding its standard deviation. The measurement repeatability is mainly limited by the signal instability and the  $1\text{-}\mu\text{m}$  scanning step of the stage during measurements.

#### 4.5 Measurement Depth

The measurement depth mainly depends on: 1. the collection of reflected light from the interface; and 2. the optical dispersion match between two optical arms. The reflected light is limited by numerous factors such as the structures and numerical aperture of optical probe, optical dispersion caused by the top layer, the mechanical property of the interface (smooth or rough), and the perpendicularity between the interface and the optical axis of the probe. The dispersion match between arms refers to the fact that the optical dispersion in two arms has to be matched to form a relatively good interference signal. As it is hard to give an exact depth limit for this technology, we estimated it with two representative materials. The first example is shown in Fig. 4. The measurement depth is about 4 mm for the PDMS sample with a dispersion compensation slide and

the probe composed of a collimator and a focusing lens. The second example is shown in Fig. 6, in which the signal has a large variation when the OCT scans a PC-based microfluidic device from bottom to top. There is no compensation slide and focusing lens (i.e., only collimator in the probe). The sample's cover surface (top), substrate (bottom), and channel top and floor are evident. Considering the refractive index of PC 1.585,<sup>24</sup> the equivalent physical thickness of the whole sample in air is 3.1 mm. Since the signal at the substrate has been relatively small, we estimated the measurement depth when measuring a PC sample without compensation slide and using collimating light should be greater than 3 mm.

## 5 Conclusions

An optical fiber-based OCT device was reported for inspection of the bonding quality of microfluidic devices. With this OCT, a series of microfluidic devices bonded with thermal method, oxygen plasma, and adhesive tape were successfully inspected and measured. The sealing completeness and geometry deformation was emphasized. The system sensitivity is 0.04 pW (the effective light intensity incident onto the photodetector from the sample), and the SNR is 59 dB. The axial resolution of tomographic imaging is  $6\ \mu\text{m}$  in air and the lateral resolution is estimated as  $20\ \mu\text{m}$ . The measurement repeatability of the topographic profile is  $1.7\ \mu\text{m}$  ( $3\sigma$ ). Although the OCT system has some tolerance in variations of different materials, the cover layer thickness should be generally less than 4 mm in order to obtain clear images of the buried structures. The study also revealed that the pressure bonding methods such as adhesive tape or thermal method, easily leads to the geometry deformation of the microfluidic devices.

The future work will mainly focus on the improvement of the OCT performance: 1. Improve the system sensitivity and SNR, as well as decrease the perpendicularity sensitivity between the measurement probe and the sample surface. It can be implemented by applying the dynamic focusing or focus tracking technique and by changing the optical probe type. The end target is to increase the signal intensity collected from the buried interface. 2. Improve the spatial resolution, especially the lateral resolution and the depth resolution in the topographic image. This will be implemented by changing the type of probes and improving the system stability. 3. Image processing work. Any signal processing algorithms beneficial in enhancing the weak signal in the tomographic image are valuable to explore.

#### Acknowledgments

The authors would like to thank Ms. Li Zhao in Singapore Institute of Manufacturing Technology (SIMTech) for making programs for stage control and data collection. The authors also thank Dr. Jianhong Zhao in SIMTech, Dr. Todd Thorsen and Hayden Taylor in MIT, and Ms. Jing Liu at Nanyang Technological University for providing the measurement samples. Zhiguang Xu and Shiguang Li have equally contributed to this work.

#### References

1. M. R. Bennett and J. Hasty, "Microfluidic devices for measuring gene network dynamics in single cells," *Nat. Rev. Genet.* **10**, 628–638 (2009).

2. N. S. Satarkar, W. Zhang, R. E. Eitel, and J. Z. Hilt, "Magnetic hydrogel nanocomposites as remote controlled microfluidic valves," *Lab Chip* **9**, 1773–1779 (2009).
3. D. Dutta, A. Ramachandran, and D. T. Leighton, Jr., "Effect of channel geometry on solute dispersion in pressure-driven microfluidic systems," *Microfluid Nanofluid* **2**, 275–290 (2006).
4. X. Zhu, G. Liu, Y. Guo, and Y. Tian, "Study of PMMA thermal bonding," *Microsyst. Technol.* **13**, 403–407 (2007).
5. M. A. Eddings, M. A. Johnson, and B. K. Gale, "Determining the optimal PDMS–PDMS bonding technique for microfluidic devices," *J. Micromech. Microeng.* **18**, 067001 (2008).
6. J. J. Shah, J. Geist, L. E. Locascio, M. Gaitan, M. V. Rao, and W. N. Vreeland, "Capillarity induced solvent-actuated bonding of polymeric microfluidic devices," *Anal. Chem.* **78**(10), 3348–3353 (2006).
7. S. Schlautmann, G. A. J. Besselink, G. R. Prabhu, and R. B. M. Schaasfoort, "Fabrication of a microfluidic chip by UV bonding at room temperature for integration of temperature-sensitive layers," *J. Micromech. Microeng.* **13**, S81–S84 (2003).
8. A. W. Martinez, S. T. Phillips, and G. M. Whitesides, "Three-dimensional microfluidic devices fabricated in layered paper and tape," *PNAS* **105**(50), 19606–19611 (2008).
9. G. Mehta, J. Lee, W. Cha, Y. C. Tung, J. J. Linderman, and S. Takayama, "Hard top soft bottom microfluidic devices for cell culture and chemical analysis," *Anal. Chem.* **81**, 3714–3722 (2009).
10. [http://www.keyence.com/products/measure/laser/lt9000/lt9000\\_applications\\_2\\_1.php](http://www.keyence.com/products/measure/laser/lt9000/lt9000_applications_2_1.php) (August 2010).
11. [http://www.nanotech.net/ntne2006/press\\_releases/Veeco\\_Module\\_for\\_Measuring\\_Trough\\_Transmissive\\_Media.pdf](http://www.nanotech.net/ntne2006/press_releases/Veeco_Module_for_Measuring_Trough_Transmissive_Media.pdf) (February 2011).
12. A. Mishra, A. Wong, K. Bizheva, and D. A. Clausi, "Intra-retinal layer segmentation in optical coherence tomography images," *Opt. Express* **17**(26), 23719–23728 (2009).
13. M. Stehouwer, F. D. Verbraak, H. de Vries, P. H. B. Kok, and T. G. van Leeuwen, "Fourier domain optical coherence tomography integrated into a slit lamp; a novel technique combining anterior and posterior segment OCT," *Eye* **24**, 980–984 (2010).
14. C. Xi, D. L. Marks, D. S. Parikh, L. Raskin, and S. A. Boppart, "Structural and functional imaging of 3D microfluidic mixers using optical coherence tomography," *PNAS* **101**(20), 7516–7521 (2004).
15. S. G. Li, J. Liu, N. T. Nguyen, Z. P. Fang, and S. F. Yoon, "Measurement of buried undercut structures in microfluidic devices by laser fluorescent confocal microscopy," *Appl. Optics* **48**(33), 6432–6441 (2009).
16. M. Pircher, E. Götzinger, and C. K. Hitzenberger, "Dynamic focus in optical coherence tomography for retinal imaging," *J. Biomed. Opt.* **11**(5), 054013 (2006).
17. G. J. Tearney, M. E. Brezinski, J. F. Southern, B. E. Bouma, M. R. Hee, and J. G. Fujimoto, "Determination of the refractive index of highly scattering human tissue by optical coherence tomography," *Opt. Lett.* **20**(21), 2258–2260 (1995).
18. M. D. Levenson, B. A. Paldus, T. G. Spence, C. C. Harb, J. S. Harris, Jr., and R. N. Zare, "Optical heterodyne detection in cavity ring-down spectroscopy," *Chem. Phys. Lett.* **290**, 335–340 (1998).
19. R. C. Haskell, D. Liao, A. E. Pivonka, T. L. Bell, B. R. Haberle, B. M. Hoeling, and D. C. Petersen, "Role of beat noise in limiting the sensitivity of optical coherence tomography," *J. Opt. Soc. Am. A* **23**(11), 2747–2755 (2006).
20. T. Yoshino, M. R. Ali, and B. C. Sarker, "Performance analysis of low-coherence interferometry, taking into consideration optical beat noise," *J. Opt. Soc. Am. B* **22**(2), 328–335 (2005).
21. B. M. Hoeling, A. D. Fernandez, R. C. Haskell, E. Huang, W. R. Myers, D. C. Petersen, S. E. Ungersma, R. Wang, M. E. Williams, and S. E. Fraser, "An optical coherence microscope for 3-dimensional imaging in developmental biology," *Opt. Express* **6**(7), 136–146 (2000).
22. L. Deck and P. de Groot, "High-speed noncontact profiler based on scanning white light interferometry," *Int. J. Mach. Tools Manufact.* **35**(2), 147–150 (1995).
23. D. Huang, E. A. Swanson, C. P. Lin, J. S. Schuman, W. G. Stinson, W. Chang, M. R. Hee, T. Flotte, K. Gregory, C. A. Puliafito, and J. G. Fujimoto, "Optical coherence tomography," *Science* **254**(5035), 1178–1181 (1991).
24. <http://en.wikipedia.org/wiki/Polycarbonate> (August 2010).